Publications of the Astronomical Society of the Pacific, 132:024202 (15pp), 2020 February https://doi.org/10.1088/1538-3873/ab55f1

Imaging Polarimetry of the 2017 Solar Eclipse with the RIT Polarization Imaging Camera

Dmitry Vorobiev[1], Zoran Ninkov[2], Lee Bernard[3], and Neal Brock[4]
[1] Laboratory For Atmospheric and Space Physics University of Colorado 1234 Innovation Drive Boulder, CO 80303, USA; dmitry.vorobiev@lasp.colorado.edu
[2] Center for Imaging Science Rochester Institute of Technology 54 Lomb Memorial Drive Rochester, NY 14623, USA
[3] University of California, Santa Cruz 1156 High St Santa Cruz, CA 95064, USA
[4] 4D Technology Corporation 3280 E. Hemisphere Loop, Suite 146 Tucson, AZ 85706, USA
Received 2019 September 27; accepted 2019 November 11; published 2020 January 13

Abstract

Micropolarizer-based sensors are dramatically smaller and more mechanically robust than other polarimeters with similar spectral response and snapshot capability. To determine the suitability of these new polarimeters for astronomical applications, we developed the RIT Polarization Imaging Camera to investigate the performance of these devices, with a special attention to the low signal-to-noise regime. We found that, using the current calibration, RITPIC is capable of detecting polarization signals as small as ∼0.3%. To demonstrate the stability of RITPIC's calibration and its extreme portability, we performed imaging polarimetry of the Solar corona in Madras, Oregon during the total Solar eclipse of 2017. The maximum polarization we measured was ∼47% in the blue and red color channels, which agrees well with the maximum value predicted for a Thomson scattering corona. Similarly, we found no strong deviations in the angle of linear polarization from the tangential direction. The relative ease of data collection, calibration, and analysis provided by these sensors suggest than they may become an important tool for a number of astronomical targets.

Key words: eclipses – instrumentation: detectors – instrumentation: polarimeters – techniques: polarimetric – polarization – Sun: corona

Online material: color figures

1. Introduction

A total Solar eclipse is an awesome spectacle, which offers a rare opportunity for scientific observations that cannot be made otherwise. The most striking feature of a total Solar eclipse is the appearance of the Solar corona, which is otherwise too faint to be seen through the foreground of the daylight sky. Although the invention of the coronagraph allowed much of the corona to be observed without the aid of the Moon, the sky foreground remains a formidable adversary. Even the coronagraphs of the Large Angle Spectroscopic Coronagraph instrument on the space-based *Solar and Heliospheric Observatory* are restricted by diffraction and scattering effects to coronal regions further than 1.1 $R_{\odot}$ from the Solar center (Brueckner et al. 1995). A total eclipse provides access to coronal regions that cannot otherwise be observed.

Of particular interest, is the polarization of the corona. Near the Sun ($<10\ R_{\odot}$), the coronal brightness can be attributed to Thomson scattering of chromospheric photons off the free electrons of the *K* corona and the more complex scattering off dust particles that make up the *F* corona. Although the *F* corona only becomes comparable in intensity to the *K* corona at a radial distance of $\geqslant 5\ R_{\odot}$, it has been demonstrated by van de Hulst (1950) that along the line of sight, light from the *F* corona dilutes the high intrinsic polarization (60%–70%) of the *K* corona, resulting in observed peak values of 40%–50% (in the equatorial regions). Despite the difficulty of separating the contributions from these two components, the polarized brightness of the corona offers a unique probe of the electron density of the *K* corona (Minnaert 1930; van de Hulst 1950; Quémerais & Lamy 2002).

The path of a Solar eclipse does not usually coincide with the location of an established observatory, which requires the motivated observer to travel with her equipment. In the past, eclipse observations have been made with the naked eye (for example, Arago 1856), photographic film (Koutchmy & Schatten 1971; Koutchmy et al. 1993; Kim et al. 2017), and, more recently, electronic sensors (Skomorovsky et al. 2012). The nonlinear response of photographic film offers a large dynamic range, which is critical to observations of the corona, whose brightness changes by a factor of >1000 over a distance of just a few Solar radii. However, that same nonlinearity is detrimental to polarimetric efforts, which rely on accurate, quantitative comparisons of brightness obtained through several polarimetric channels.

Polarization-sensitive imaging arrays (Nordin et al. 1999; Brock et al. 2011; Vorobiev et al. 2018) are an attractive

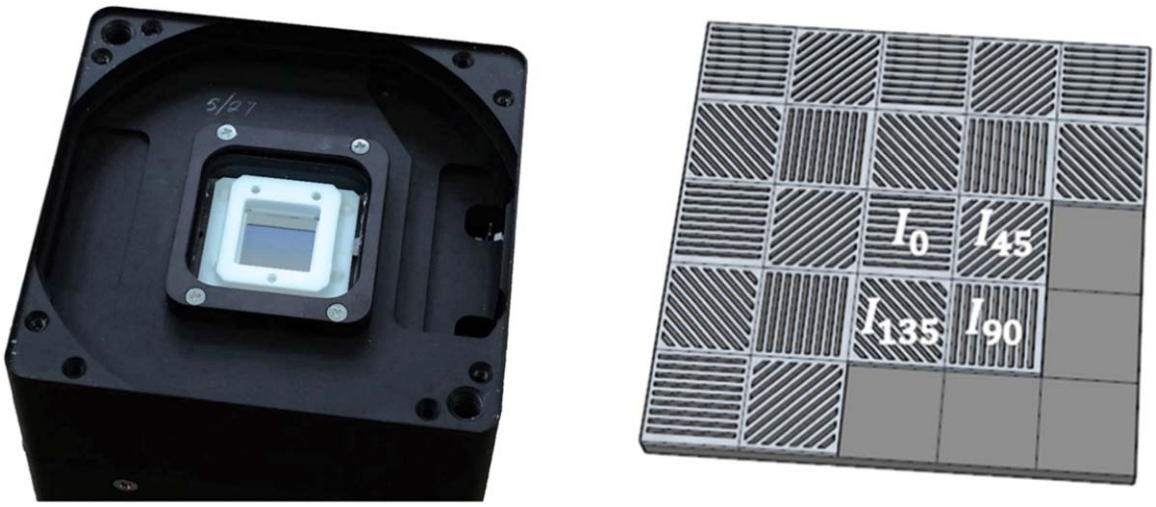

Figure 1. Left: the RIT Polarization Imaging Camera uses a KAI-04070 interline CCD from On Semiconductor, which is aligned with a micropolarizer array from Moxtek, Inc, by 4D Technology. The polarization sensor is housed in a cooled scientific MicroLine camera from Finger Lakes Instrumentation. Right: a schematic representation of the polarization sensor, where each pixel of the imaging sensor is covered by a single wiregrid linear polarizer. The intensities measured by a set of 4 pixels with different angles (0°, 45°, 90°, 135°) are demodulated to obtain the Stokes parameters. For RITPIC, the micropolarizer array is ahead/above the sensor and microlens array.
(A color version of this figure is available in the online journal.)

platform for eclipse polarimetry, due to their small size and ease of use. In this work, we present our efforts perform broadband imaging polarimetry of the Solar corona, during the total solar eclipse of 2017 August 21. We present our calibration approach and our measurements of the degree and angle of linear polarization (AOLP), with an emphasis on overall polarimetric sensitivity (i.e., "uncertainty").

2. Polarization-sensitive Imaging Arrays

Pixelated polarization sensors represent the most commercially successful and mature implementation of division-of-focal plane polarimeters (see reviews by Tyo et al. 2006 and Snik et al. 2014) to date. These devices employ micropolarizer arrays to modulate the intensity of light on a per-pixel basis (Figure 1, Right). Their key advantages are the ability to sample the electric field along several orientations in a single snapshot, compactness, ease of use, and the stability of their calibration (Vorobiev et al. 2018). In 2019, there are two variants of polarization sensors on the market: (1) Commercial off-the-shelf imaging sensors that are aligned and bonded to a micropolarizer array by a third party; (2) CMOS sensors (such as the IMX250MZR) from Sony, which include the micropolarizer array as part of the semiconductor fabrication process, under the microlens array. The RIT Polarization Imaging Camera (RITPIC) used to make the observations in this paper employs the former approach, with the alignment performed by 4D Technology.

Figure 2. The polarimetric system used to observe the total eclipse of 2017 consisted of the RIT Polarization Imaging Camera, filter wheel and focuser from Finger Lakes Instrumentation, and a Takahashi FSQ 530 mm $f/5$ refracting telescope, on an equatorial mount from Software Bisque. Here the system is shown on the roof the Chester F. Carlson Center for Imaging Science at RIT, in Rochester, NY.
(A color version of this figure is available in the online journal.)

3. Polarimetry of the Solar Corona

To perform polarimetry of the Solar corona, we used a 530 mm $f/5$ Takahashi FSQ 4-element refractive telescope and the RITPIC (Vorobiev et al. 2018; see Figure 2). This resulted in a plate scale of $2\farcs88$ per pixel and $5\farcs76$ per image element/superpixel. The resulting field of view was $\sim 63' \times 63'$, i.e., roughly $4\,R_\odot$. In this case, the seeing disk is severely undersampled, with only ~0.5–1 superpixel per FWHM. This focal length was chosen regardless, because a field of view

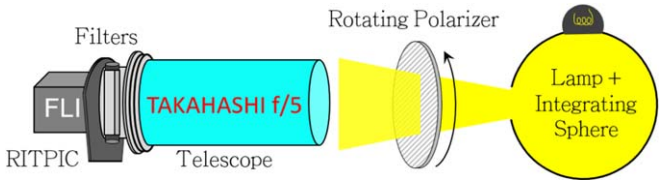

Figure 3. The instrumental response of each pixel of the RIT Polarization Imaging Camera was characterized by illuminating the entire system with polarized light, using an integrating sphere and a rotating polarizer. The relative throughput, polarization efficiency, and orientation were determined by model fitting, as described in Vorobiev et al. (2018).
(A color version of this figure is available in the online journal.)

Table 1
The Contrast Ratio of the Analyzer (Model PPL04C) used to Produce Polarized Light for the Characterization of RITPIC and the Corresponding Polarization Purity of the Light

Wavelength nm	Contrast	Polarization Purity (%)
400	392 ± 19:1	99.74 ± 0.01
500	1160 ± 25:1	99.913 ± 0.002
600	1786 ± 21:1	99.944 ± 0.001
700	2473 ± 44:1	99.959 ± 0.001

$\gtrsim 2\,R_\odot$ was needed to study the structure of the corona in the region of 1–1.5 $R_\odot$.

3.1. Instrumental Characterization

To prepare for observations in the field, the instrumental response of each pixel was determined for the entire system (telescope, filters, and RITPIC) (Figure 3), using an integrating sphere and a rotating linear polarizer. The relative throughput, polarization efficiency, and relative orientation of every pixel was determined by moving the rotating polarizer over a range of 200°, in 1° increments, and acquiring several images at each position. For this characterization we used a wire grid polarizer from Moxtek, Inc.; the absolute angular position of the polarizer is known to $\sim 1\overset{\circ}{.}5$ and the contrast ratio in the relevant calibration bands is given in Table 1. This procedure is similar to that presented in Vorobiev et al. (2018), where the response non-uniformity of RITPIC is discussed at length. In this case, the entire system was characterized at once, including the telescope, bandpass filters, and the micropolarizer camera itself.

Using the characterization obtained in this way, we analyzed a set of unpolarized and polarized flat field images to estimate the instrumental polarization of the entire system. Analysis of unpolarized flats (generated using an integrating sphere only) showed that the minimum polarization estimated by the system varied from 0.61% ± 0.1% in the blue channel, to 0.67% ± 0.1% in the red channel. Analysis of polarized flats

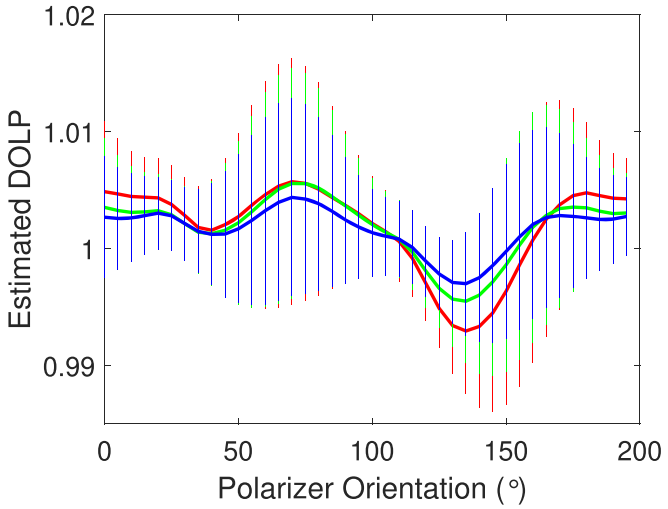

Figure 4. Polarimetric analysis of polarized flat field images, over a range of polarization angles, performed with the Bessel *B*, *V*, and *R* filters, shown here with correspondingly colored lines. The error bars here represent the standard deviation of all pixels in a single flat field, i.e., the spatial variability.
(A color version of this figure is available in the online journal.)

(with the polarization indicated in Table 1), reveals some residual instrumental effects in our demodulation process (Figure 4). The estimated degree of linear polarization (DOLP) for the polarized flats varies between 99.5% and 100.5%, depending on the angle of the incident polarization. Additionally, the spatial variability (indicated by the error bars in Figure 4) in each frame is ∼±1%, with better performance in the blue channel, than in the red.

We attribute the angle-dependence of our instrumental response to the fidelity of our characterization process. A systematic error in the determination of the relative throughput or orientation differences between micropolarizer pixels would lead to a similar response. Overall, we expect this systematic uncertainty to decrease as the degree of polarization of incident light decreases, with the deviations shown here representing the upper limits.

3.2. Image Acquisition

Our observations were made from Madras, OR, on 2017 August 21. We acquired sequential images in the Bessel *B* and *R* passbands, using a range of exposure times. The intensity of the corona changes by a factor of 200 from the edge of the solar disk to a distance of 1 $R_\odot$ away (Figure 5). Our sensor's limited dynamic range required the use of exposure bracketing (a.k.a. high dynamic range imaging) to image the corona with sufficient SNR, while remaining in the linear operational regime of the CCD. A total of 42 frames (in seven sequences of 6 exposures each) were acquired during totality; a summary of target regions, exposures, and passbands is given in Table 2. In

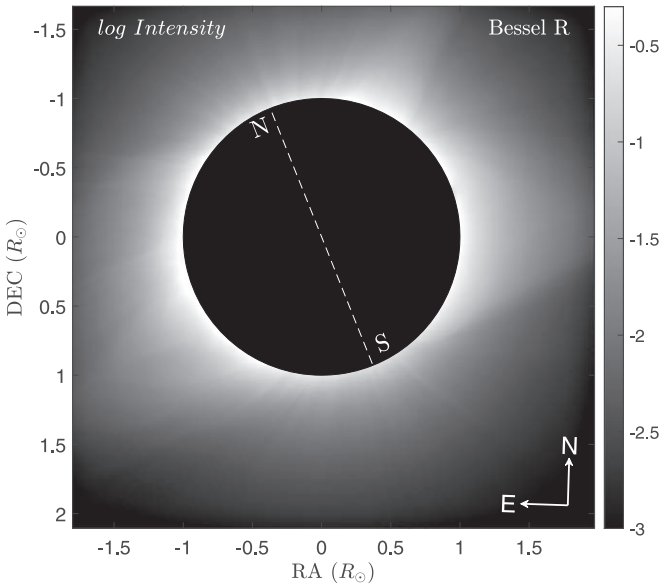

Figure 5. This map of the intensity of the corona (Stokes *I*) was made by median-combining the set of 7 individual Stokes *I* HDR maps, in the Bessel *R* band. This set of exposures spans the entire duration of totality. The dashed line across the Solar/Lunar disk identifies the Solar axis, with the Solar north and south poles indicated. The arrows in the bottom right corner indicate the directions on the celestial sphere; Note the celestial North pole is tilted w.r.t. the *y*-axis of our images by ∼2°, toward West.

this way, we obtained a full set of observations at 7 instances over the duration of totality.

We acquired observations at four different exposure levels (two for the *B* filter), with seven images per exposure level, during totality (see Table 2). First, maps of the normalized Stokes parameters, q and u, were calculated for each of the seven images and combined using a median. This resulted in four median maps, corresponding to the four exposure levels. Then, regions of high (photometric) signal were identified in each map. Pixels with a photometric SNR < 35 and pixels close to saturation were flagged as "bad." The remaining high SNR pixels in the four median maps were combined using a weighted mean; the SNR of each pixel in each map was used as its weight (see Section 3.5).

3.3. Polarization of the Solar Corona

In this section, we present the results of our linear polarimetry of the Solar corona. First, we show the maps of the normalized Stokes parameters, q and u, in the instrumental reference frame. These maps were made by obtaining the median of the 7 HDR frames acquired through the duration of totality (each consisting of 2 exposures for the *B* channel and 4 exposures for the *R* channel). The resulting composite maps are shown in Figure 6. The distribution of the normalized Stokes parameters in the corona shows the overall tangential

Table 2
Exposures Acquired During the 2017 August 21 Total Solar Eclipse with the RIT Polarization Imaging Camera

Filter	Exposure Time (s)	# of Frames	Part of Corona to be Sampled
B	0.05	7	1.1–1.25 $R_\odot$
	1	7	1.25–1.5 $R_\odot$
R	0.01	7	1–1.1 $R_\odot$
	0.05	7	1.1–1.25 $R_\odot$
	1	7	1.25–1.5 $R_\odot$
	5	7	1.5–2 $R_\odot$

Note. The images were acquired in sets of 6 (*B05*, *B1*, *R01*, *R05*, *R1*, *R5*) exposures, seven times throughout the duration of totality.

polarization structure, as well as some smaller scale features. The peak fractional polarization is ∼47% in both q and u. Overall, the fractional polarization in the *B* channel appears to be slightly higher than through the *R* filter.

Using the normalized Stokes parameters, we calculate the DOLP and the AOLP (Figure 7). Although DOLP is a biased estimator of the fractional polarization, it is useful because it is independent of any reference frame, allowing for straightforward comparison of measurements made by different observers/instruments.

At a glance, the structure of the DOLP is similar to that of the overall intensity (Figure 5). However, there exist several differences. Most significantly, the intensity of the corona (Stokes *I*) peaks near the limb and rapidly decreases with increasing distance from the Sun. Meanwhile, the DOLP is not maximal near the limb (∼30%), and peaks at a distance of $\sim 1.5\,R_\odot$. Furthermore, the rate at which the intensity and DOLP decrease is dramatically different. Near the edges of our field of view, the intensity has decreased by a factor of ∼500, whereas the DOLP has only decreased by a factor of ∼2.

3.4. Sky Polarization

As part of an extensive observing campaign prepared for the 2017 eclipse, all-sky polarimetry by Eshelman et al. (2018), Shaw et al. (2019) revealed that the sky in the direction of the Sun is polarized in a large band, at the ∼40% level, with lower polarization very near the Sun. This pattern is significantly different than the typical symmetric polarization pattern, which is minimal toward the Sun, and increases to a peak at ∼90° away from the Sun. Our observations have the sufficient spatial resolution and dynamic range to measure the foreground sky polarization across the Solar/Lunar disk. The degree of polarization for the Bessel *B* and *R* channels are shown in Figure 8. The linear polarization of the sky is clearly defined up to a distance of $\sim 0.5\,R_\odot$ from the center of the Solar/Lunar disk, where it begins to become comparable in intensity to the

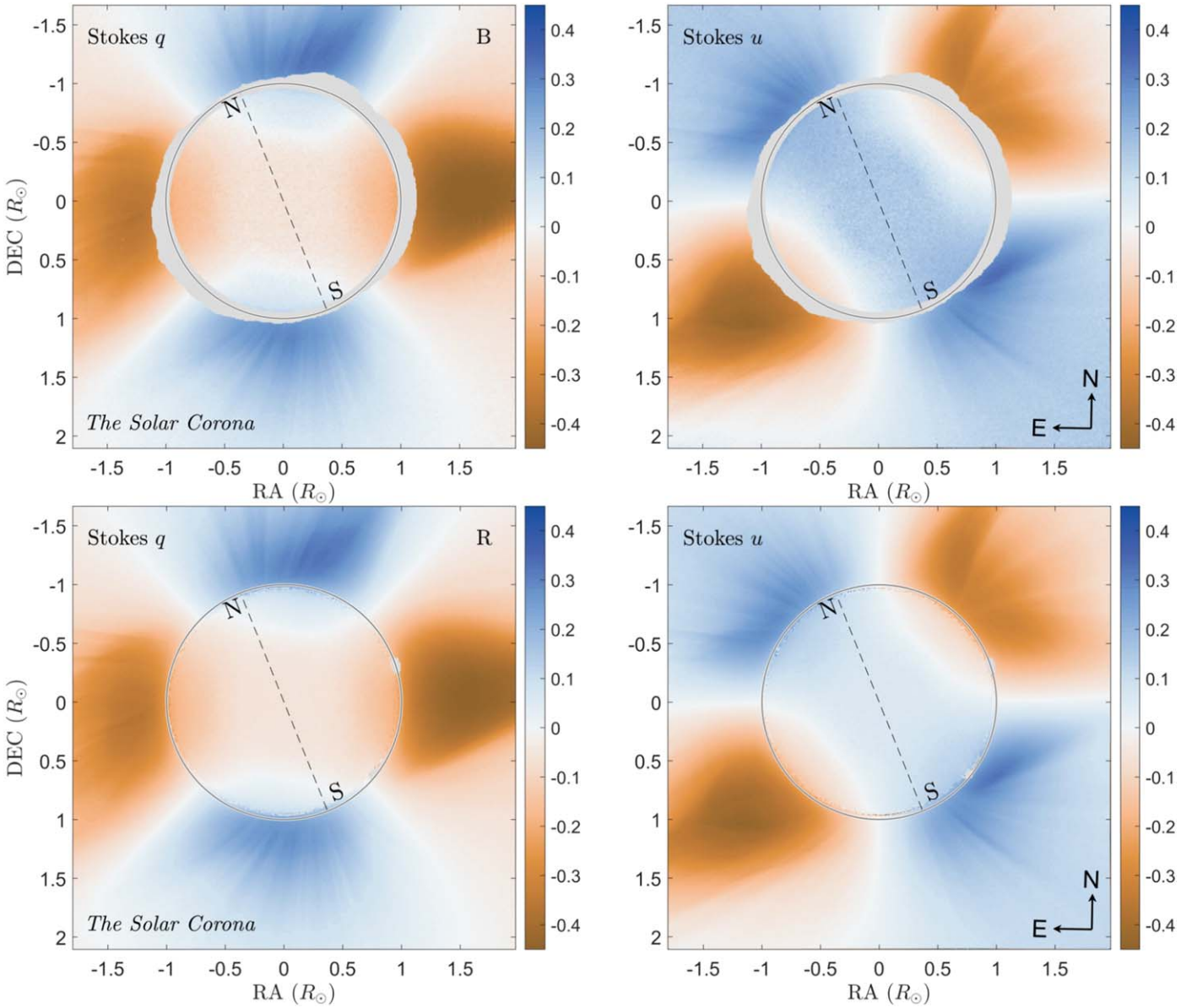

Figure 6. Maps of the normalized Stokes parameters, q and u (in the instrument's reference frame), show the polarization structure of the Solar corona in the Bessel B (Top) and Bessel R (Bottom) filter passbands. The general tangential polarization of the corona, as well as some smaller scale features are clearly seen.
(A color version of this figure is available in the online journal.)

scattered light from the solar corona, which maintains its characteristic circular pattern. The regions where the sky and coronal light have parallel and orthogonal polarization are clearly distinguishable by regions of maximal and minimal fractional polarization, respectively.

The measurements in the blue and red channels exhibit some systematic differences. First, the degree of polarization in the blue channel (as measured in the circled region of Figure 8) is higher than in the red channel, at 0.16 ± 0.013 and 0.08 ± 0.005, respectively. Second, the angle of polarization of the sky foreground differs between the two channels by $\sim 11 \pm 2°$. The angle of polarization of the blue light is more closely aligned with the scattering plane, with an average deviation of $\sim 7°$ (toward celestial North).

We believe these measurements accurately reflect the polarization state of the sky and are not an instrumental effect. We have been unable to find similar measurements in the literature to perform a direct comparison; most sky

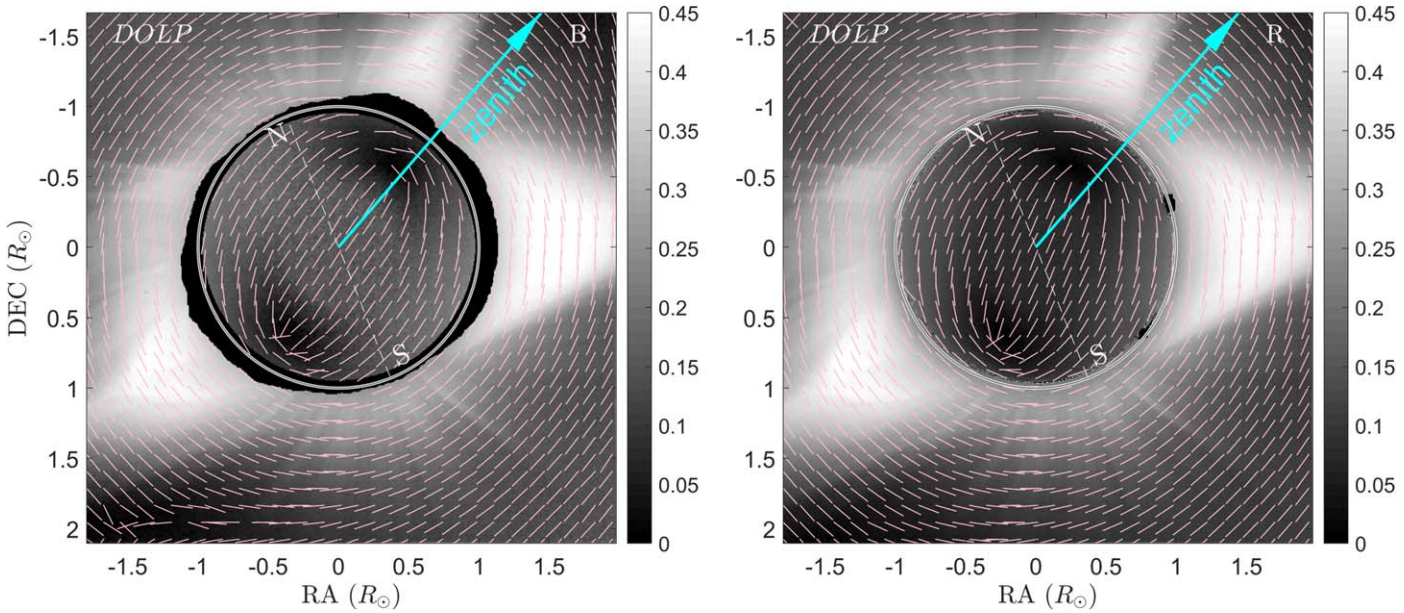

Figure 7. The degree of linear polarization (DOLP) and the angle of linear polarization (AOLP) in the instrumental reference frame are shown (for the Bessel *B* (Left) and Bessel *R* (Right) filters) as an intensity map and vector plot, respectively.
(A color version of this figure is available in the online journal.)

polarization studies performed in the past used either all-sky imaging (Pomozi et al. 2001; Eshelman 2018; Eshelman et al. 2018; Shaw et al. 2019) or pointed observations, focused on the solar meridian and the anti-solar point specifically (Dandekar & Turtle 1971). Our measurements in the blue channel roughly agree with those of Eshelman (2018), within the respective measurement uncertainties. However, the degree of polarization in the red channel differs significantly between their measurements and ours, at ∼0.24 and ∼0.08, respectively.

The source of this discrepancy is not clear. However, it may be due to the different local conditions under which the two measurements were taken. The sky over Madras, Oregon had smoke clouds from a nearby wildfire and some thin high altitude cirrus clouds. Conversely, the sky over Rexburg, Idaho, where the Eshelman (2018) observations took place, were relatively clear. In the future, it may be useful to combine all-sky imaging and more pointed narrow-field observations of sky polarization during a total Solar eclipse.

Because we acquired seven complete sets of measurements throughout the duration of totality, we are able to investigate the temporal evolution of the sky foreground (Figure 9). Throughout totality, the degree of polarization in the blue channel increased slightly, but steadily, while the polarization in the red channel remained mostly constant. Conversely, a much larger change in the angle of polarization was measured in the red channel as the eclipse progressed.

3.4.1. Sky Foreground Subtraction

As part of our polarization analysis, we subtract the sky foreground early in the demodulation process. In each frame, the sky foreground is estimated by the median of the pixels in the region circled in Figure 8. We assume that in this region the polarized brightness is dominated by the sky, with minimal contribution from the scattered coronal light. In the discussion that follows, all maps have been foreground-subtracted. The foreground-subtracted polarization maps are shown in Figure 10.

Though the coronal polarization does not change dramatically, some key differences can be seen, as compared to the previous maps (Figure 7). The light behind the Lunar disk is now dominated by scattered light from the corona, which maintains its tangential orientation. The DOLP in this region is ∼23% in the *B* channel and ∼25% in the *R* channel. The AOLP throughout the field of view is more uniform without the sky foreground, especially at distances greater than $\sim 2\,R_\odot$, as can be seen in the bottom left corner of the Bessel *B* map. In the future, it would be useful to compare the sky polarization measured behind the Lunar disk to that measured at a greater distance from the Sun, for example over the range of ~ 5–$15\,R_\odot$.

3.5. Analysis of Uncertainty

In this subsection, we outline the procedure we used to obtain an estimate of the uncertainty associated with our

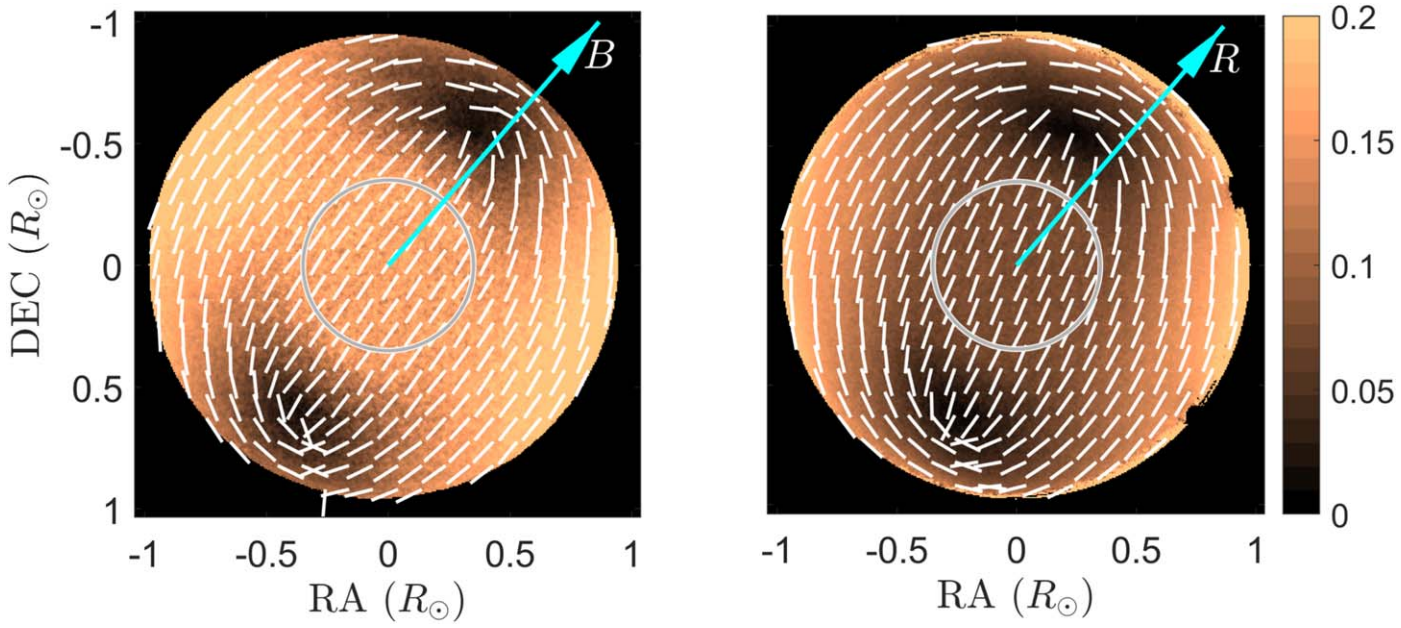

Figure 8. We measured the foreground sky polarization in the Bessel *B* (Left) and *R* (Right) filter passbands. The gray circle near the center indicates the region we assumed to be dominated by sky foreground and used for foreground subtraction in the following analysis. The median polarization in the *B* and *R* bands in this region was 0.16 ± 0.013 and 0.08 ± 0.005, respectively. The blue arrow points toward zenith.
(A color version of this figure is available in the online journal.)

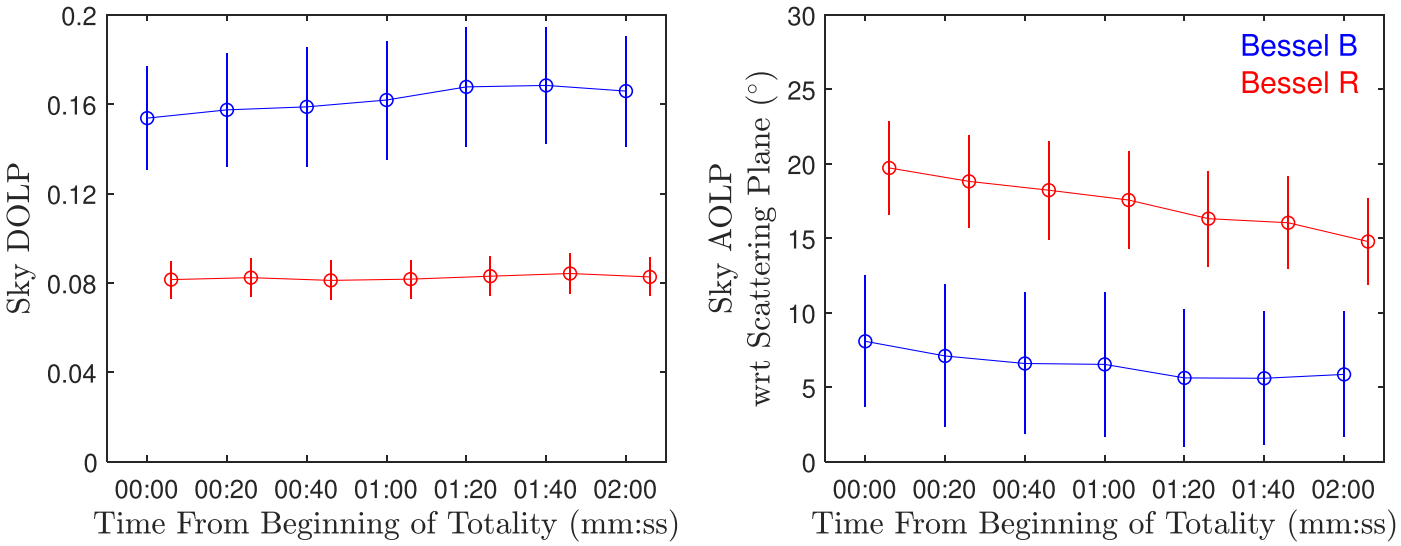

Figure 9. Degree (Left) and angle (Right) of linear polarization measured for the sky region circled in Figure 8, throughout the eclipse. The blue and red lines represent the measurements made in the blue and red channels, respectively. Note they are offset slightly in time, because the blue measurements were acquired first. The error bars represent the standard deviation of all points within the measurement region.
(A color version of this figure is available in the online journal.)

measurements of the normalized Stokes parameters and the DOLP. The Stokes parameters are estimated in each RITPIC frame on a per-pixel basis, using a linear least squares fit,

$$\hat{\boldsymbol{S}} = (\boldsymbol{X}^\top \boldsymbol{X})^{-1} \boldsymbol{X}^\top \boldsymbol{Y}, \quad (1)$$

where $\hat{\boldsymbol{S}}$ is the estimated Stokes vector (excluding the 4th element), $\boldsymbol{X}$ describes the micropolarizer performance (including contrast and orientation), and $\boldsymbol{Y}$ is the vector of corresponding pixel fluxes, in units of electrons. The uncertainties of the estimated Stokes parameters are calculated

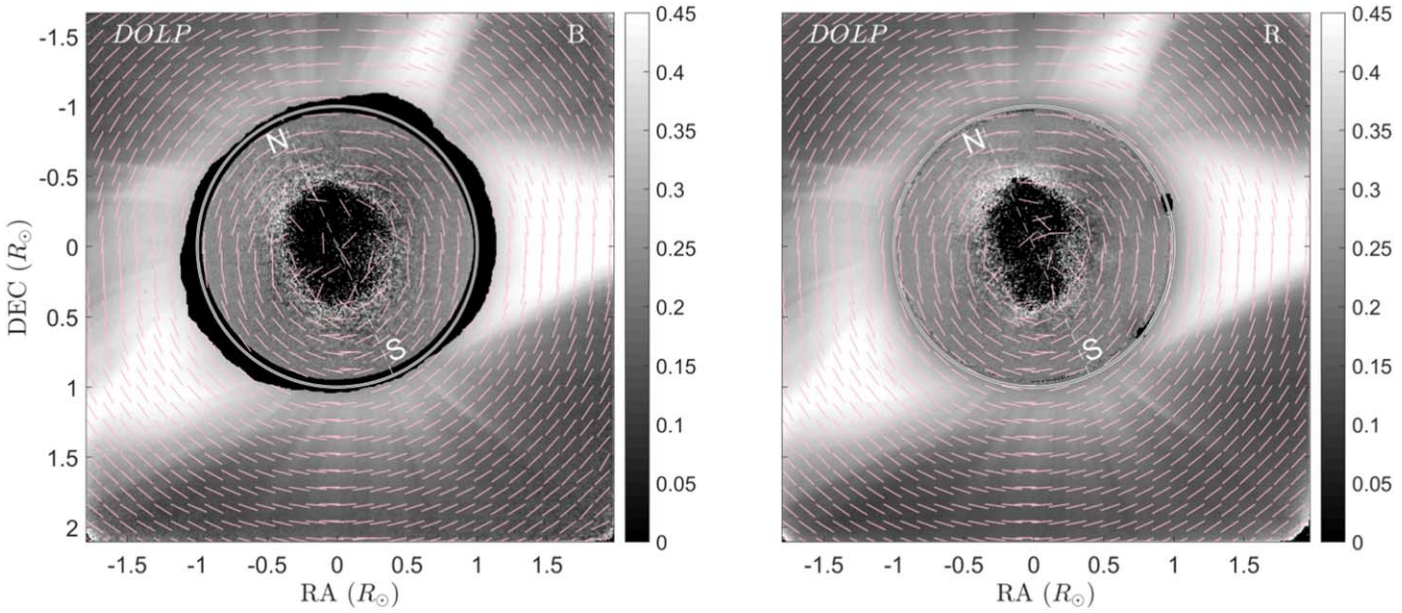

Figure 10. The degree and angle of linear polarization for the Bessel *B* and *R* channels, after the sky foreground was removed. The scattered light from the corona can be seen across much of the Lunar disk. Overall, the angle of linear polarization is more uniform across the field of view, compared to that in Figure 7. Note that North is up and East is to the left in these images.
(A color version of this figure is available in the online journal.)

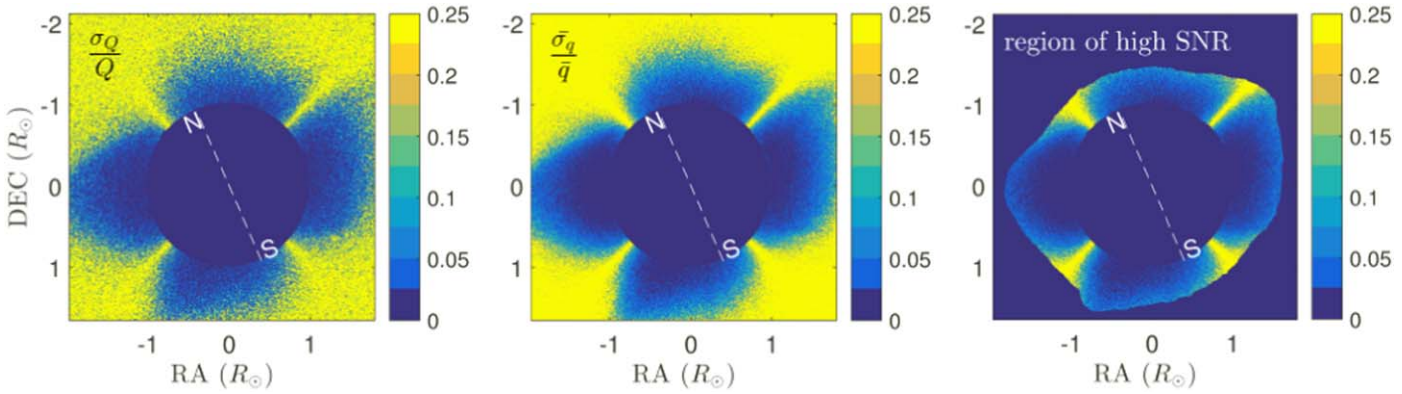

Figure 11. Left: the fractional error associated with the estimation of Stokes Q in a single 10 ms frame. Middle: the fractional error of the estimation of Stokes q, made from a set of 7 frames. Right: a region of the Stokes q map, with photometric SNR > 35 and excluding saturated pixels.
(A color version of this figure is available in the online journal.)

using analysis of residuals. The variance associated with each measurement, σ^2, is calculated using the unbiased estimator $\hat{\sigma}^2$ (Bajorski 2011) as follows,

$$\hat{\sigma}^2 = \frac{1}{n-2}\sum_{i=1}^{n}(y_i - \hat{y}_i)^2 = \frac{1}{2}\sum_{i=1}^{n}(y_i - \hat{y}_i)^2, \quad (2)$$

where $n = 4$ (the number of raw pixels used to determine the Stokes parameters), y_i is an intensity measured by the ith pixel in a set of 4, and $\hat{y}_i$ is the intensity predicted by the model $\hat{\boldsymbol{Y}} = \boldsymbol{X}\hat{\boldsymbol{S}}$. Finally, the variance of the estimated Stokes parameters is determined using the measurement variance and the micropolarizer matrix, $\boldsymbol{X}$,

$$\boldsymbol{\sigma}^2_{\hat{\mathbf{S}}} = \hat{\sigma}^2(\boldsymbol{X}^\top\boldsymbol{X})^{-1}. \quad (3)$$

This results in a map of variance for each Stokes parameter ($\hat{\sigma}_I$, $\hat{\sigma}_Q$, $\hat{\sigma}_U$,), for each data frame (Figure 11, Left). Using formal uncertainty propagation, we determine the variances of the normalized Stokes parameters: σ_q and σ_u. Next, using the set of 7 measurements, we obtain the median values of the normalized Stokes parameters and the average variance: $\bar{q}$ and $\bar{\sigma}^2_q$

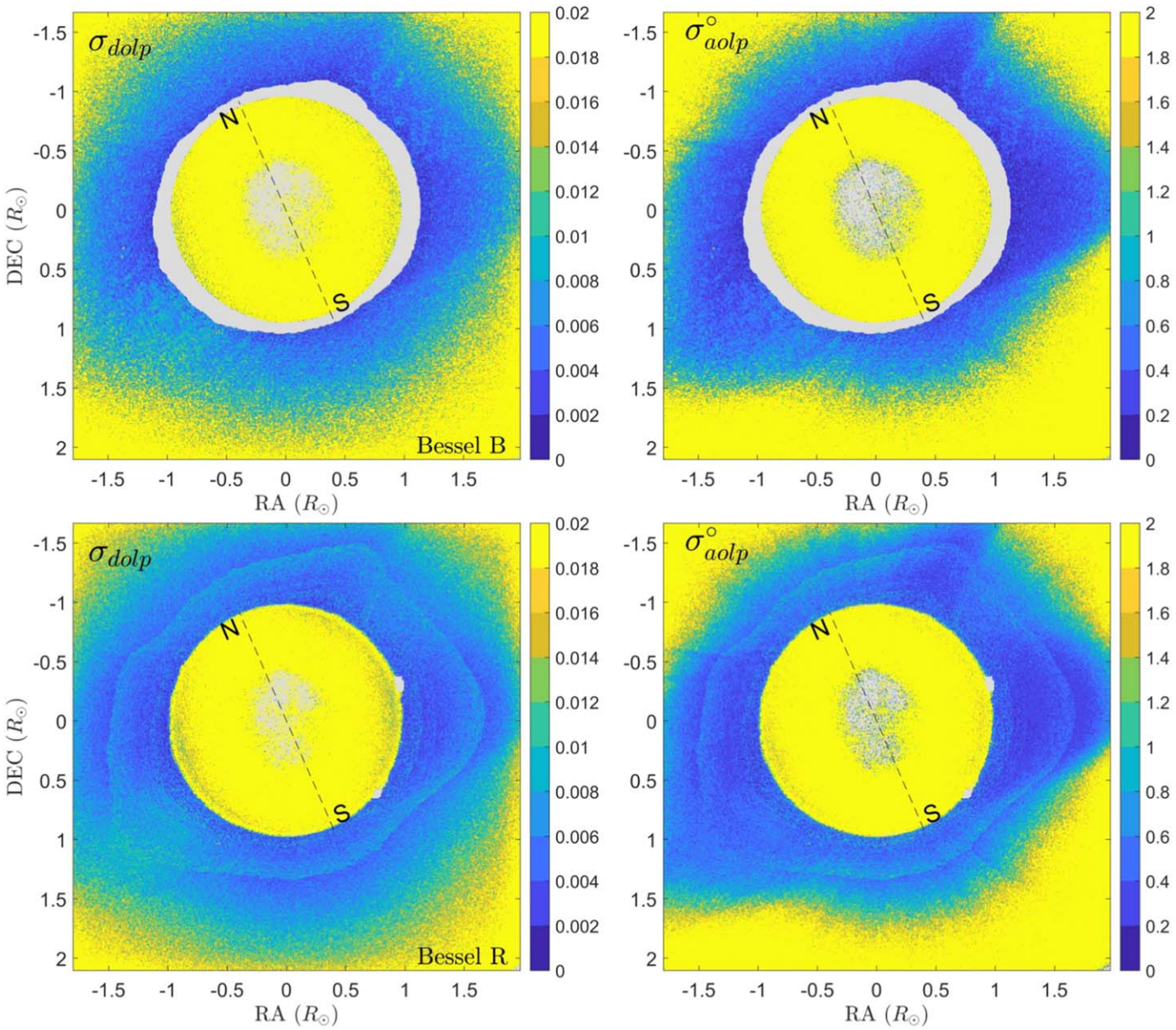

Figure 12. Left: the uncertainty of the estimation of degree of linear polarization of the corona, estimated as the standard deviation of a set of 7 HDR measurements. In regions of high polarization, the standard deviation is <1%, increasing to ∼2% near the edges. Right: the uncertainty (in degrees) of the angle of linear polarization in our measurement. Within ∼1.5 $R_\odot$, our angle measurement is precise to ∼1°. Gray pixels indicate areas of saturation or SNR < 1.
(A color version of this figure is available in the online journal.)

(Figure 11, Middle). Finally, we use the map of Stokes *I* to find regions with photometric SNR > 35 and mask off saturated pixels. The resulting region of "high quality" data for the 10 ms exposures is shown in the right panel of Figure 11.

This process is repeated for the remaining frames, with exposures of 50 ms, 1 s, and 5 s. The high SNR regions from each exposure set are combined to generate the maps shown in Figures 6 and 7. The uncertainties from high SNR regions of each exposure set are combined using a weighted mean. The weighting is determined by the SNR of each measurement. In this way, the contribution of the noisier measurements is diminished, if better data are available from a different exposure set. As a result, the uncertainties of the final measurements, σ_q and σ_u, are not the true standard deviation; however, they are still a reasonable estimate of the uncertainty of each measurement.

Lastly, we use the uncertainties σ_q and σ_u to find the uncertainty associated with the DOLP and AOLP in the corona,

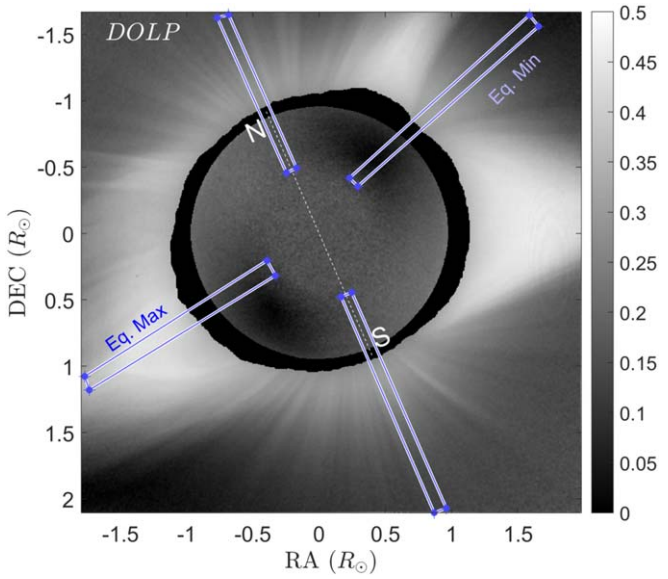

Figure 13. To compare our measurements to the predictions of the model corona of van de Hulst (1950), we acquired azimuthally averaged radial profiles in four regions: at the north and south poles, and in regions of maximal and minimal polarization near the equator.
(A color version of this figure is available in the online journal.)

$\sigma_{\rm dolp}$ and $\sigma_{\rm aolp}$, using formal (linear) uncertainty propagation. Strictly speaking, this procedure gives a biased estimate of both the fractional polarization, DOLP, and its uncertainty, $\sigma_{\rm dolp}$. However, the corona is very strongly polarized, even in areas of low polarization. This high "polarimetric SNR" (>20 across our field of view) ensures that the relative effect of the bias is small. The maps of uncertainty are shown in Figure 12. In regions where the polarization is large, our combined measurement of the fractional polarization has an uncertainty of ∼1%–3%. At distances $>1.5\,R_\odot$, the lack of signal from the corona and the sky foreground lead to rapidly increasing uncertainty. A similar trend can be seen in the estimate of the AOLP (Figure 12, Right). Where the signal is high, the angle estimation is precise to ∼1°. Further out, the uncertainty increases to ∼2°.

3.6. The Structure of the Corona

For a quick comparison of our measurements to the predictions of a Thomson scattering corona, we use the theoretical curves of van de Hulst (1950). The van de Hulst model is azimuthally symmetric, with a separate treatment for the equatorial and polar regions. This model includes both the highly polarized K corona and the weakly polarized F corona. Each parcel of coronal plasma is primarily illuminated by photons from the solar photosphere, such that at a distance R from the Solar surface, the plasma is illuminated by a "cone" that subtends the solid angle $\Omega = \frac{1}{R^2}$ on the photosphere. Very near the photosphere, the corona is illuminated significantly by photons from a large fraction of the photosphere and from many directions, leading to a fairly low average polarization. As the distance increases to $R \approx 1.5\,R_\odot$, the majority of the light is arriving from a relatively small region of the photosphere, nearly radially, resulting in the high fractional polarization of ∼60%. This high polarization fraction is predicted by van de Hulst (1950) to extend to distances of $R \approx 6\,R_\odot$, contrary to most observations. This discrepancy is usually attributed to the dilution of the highly polarized K corona by light scattered by interstellar dust particles which makes up the weakly polarized F corona.

During this eclipse, the corona showed strong polarization features in the equatorial direction, with weaker polarization (and intensity) at the poles. Large scale and small scale "streamers" are clearly visible. The DOLP of the corona peaks at ∼47% in the equatorial features, at a distance of $\sim 1.5\,R_\odot$. To perform a preliminary comparison to the van de Hulst (1950) models, four regions were chosen: one each at the north and south poles, and in areas of maximal and minimal polarization near the equatorial regions (indicated by rectangles in Figure 13). The radial profiles (Figure 14) were created by averaging the polarization in these regions, in the azimuthal direction. Four regions were chosen: one each at the north and south poles, and in areas of maximal and minimal polarization in the equatorial regions.

The maximal polarization we measured agrees well with the maximum predicted values from van de Hulst (1950). However, the polarization measured at the north and south poles is significantly higher than the model prediction. The minimally polarized regions near the equator are also more significantly polarized. The source of the discrepancy is not clear to us at this time. It is likely that the azimuthally symmetric model does not adequately account for the electron density structure in the real corona. Also, the impact of the sky foreground is difficult to rigorously quantify with the data we have available. Indeed, the sky-subtracted maps show more significant deviations from the model than the un-calibrated measurements, especially further from the Solar center. This may indicate over-subtraction of the sky foreground, because the corona intensity (and thus polarized intensity) is fainter in these regions.

3.6.1. Distribution of the Polarization Angle

The angle of polarization is tangential to the solar limb. This is shown in Figures 7 and 10. To identify any underlying structure in the AOLP, we plot the deviations of the AOLP from the purely tangential direction, denoted by the angle χ, in Figure 15. In regions of strong polarization (and high SNR), our estimate of the AOLP is consistent with the tangential direction within ∼0.°5. Where the polarization is low, like near the south east limb, the deviation increases to ∼1°. In regions further than $\sim 1.5\,R_\odot$, the deviation increases to >3°.

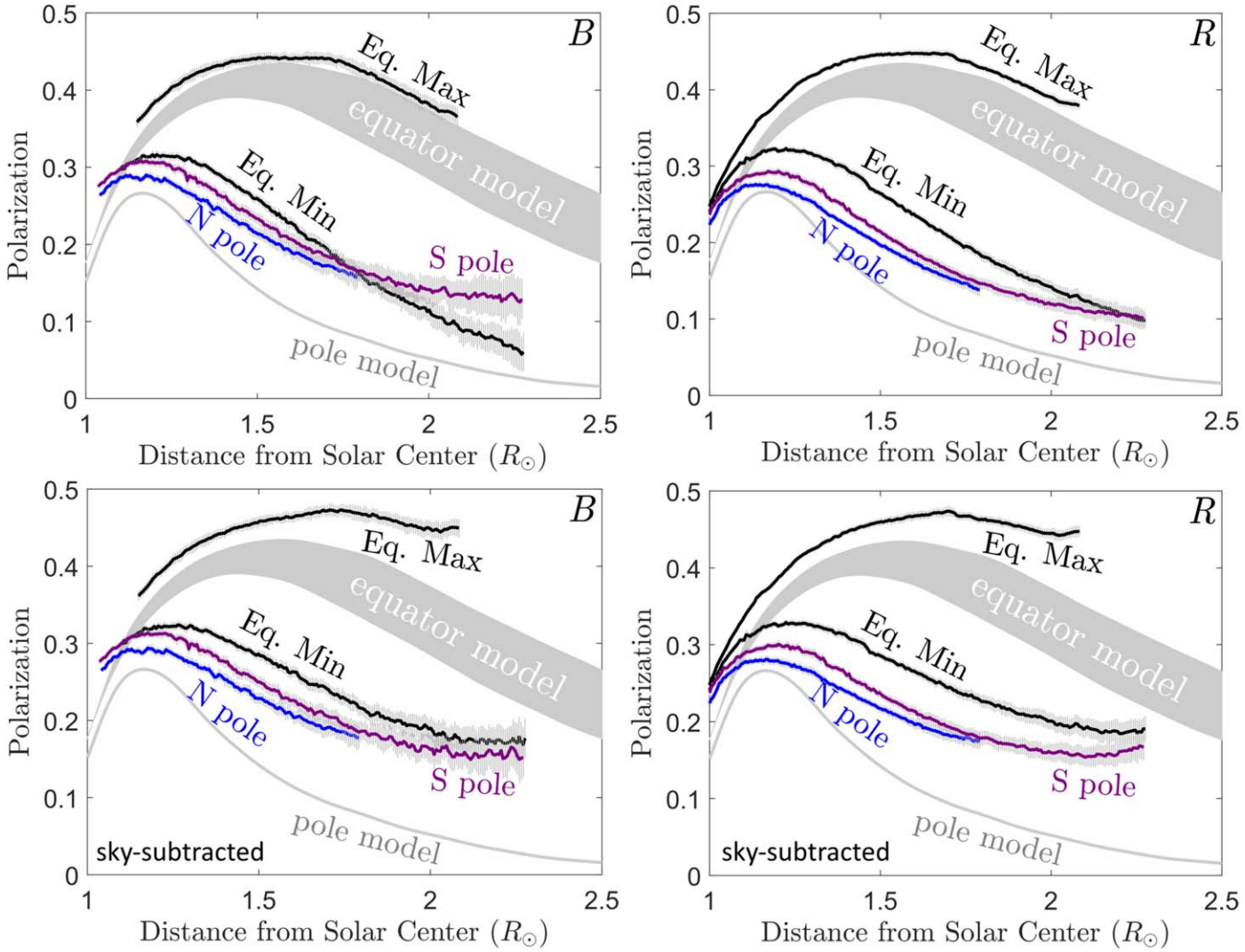

Figure 14. Our measured profiles calculated in the four regions indicated in Figure 13, plotted on top of predictions for a Thomson scattering corona from van de Hulst (1950). The maximum measured polarization does not greatly exceed the maximum value predicted by Thomson scattering, up to a distance of $\sim$1.75 $R_\odot$. However, in profiles where the sky-subtraction was performed (Bottom Row), start to deviate more significantly from the van de Hulst (1950) model at distances $>$1.5 $R_\odot$. (A color version of this figure is available in the online journal.)

4. Summary of Observations from 2017 August 21

We performed broadband imaging polarimetry of the corona in the Bessel *B* and *R* filters. During the eclipse of 2017 August 21 the corona was asymmetric, with a pronounced "Y" shape in the equatorial regions. The peak polarization was 47% $\pm$ 1%, in the arms of the "Y" structure, at a distance of $\sim$1.5 $R_\odot$. We do not measure any unexpectedly large polarization, of the kind discussed by Koutchmy & Schatten (1971) and reported more recently by Qu et al. (2013).

Deviations of the angle of polarization from the tangential direction have been reported by various groups, most recently by Skomorovsky et al. (2012), Qu et al. (2013), and Kim et al. (2017). We do not measure any deviations from the tangential direction, larger than 1°. The deviation, χ increases in areas of low SNR, at distances $\gtrsim$2 $R_\odot$. We suspect that in these regions, the measurements are becoming affected by the sky polarization. Indeed, Skomorovsky et al. (2012) admit that the strong deviations they measured are "apparently caused by the insufficient quality of [the] coronal images."

Our measurements are similar to those of Koutchmy et al. (1993), who did not measure deviations larger than 1°. Small deviations of 1°–2° have been proposed to arise from scattering by relativistic electrons by Molodensky (1973), and further developed by Inhester (2015). The precision of our angle estimation should be sufficient to detect changes of this magnitude, because the beamed emission also shows larger

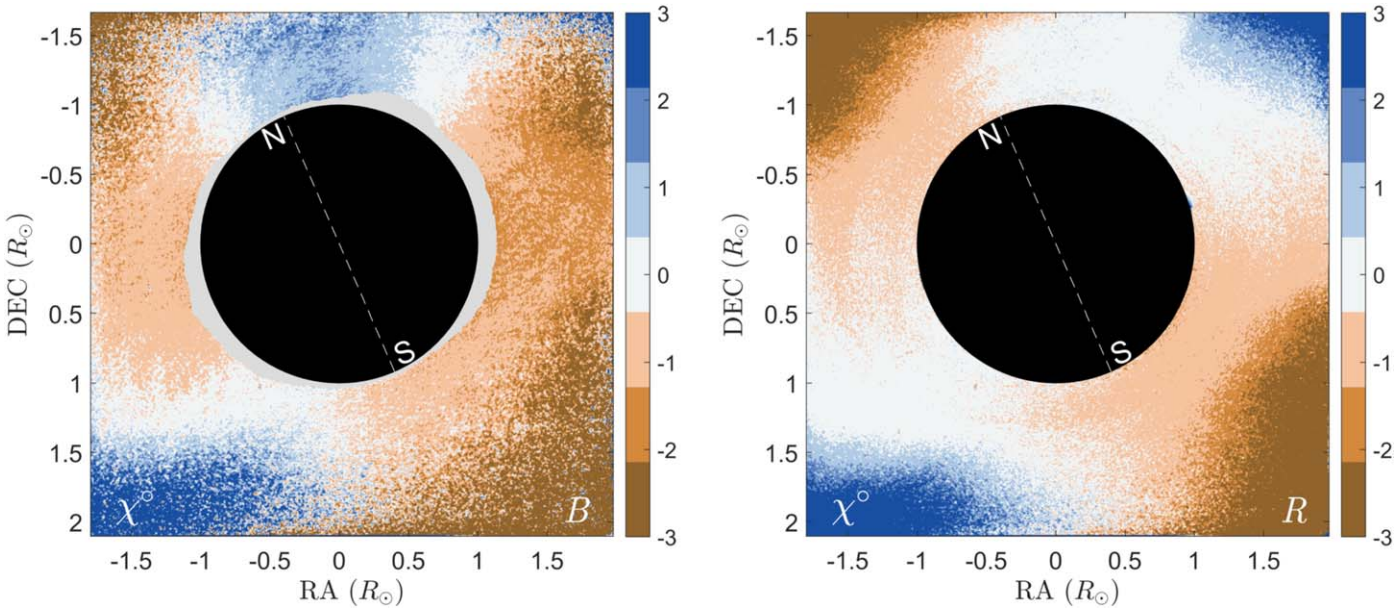

Figure 15. A map of the deviation of the angle of linear polarization from the tangential direction, in the *B* and *R* filters. Across our field of view, the AOLP follows the tangential direction, within our measurement uncertainties. The gray annulus in the Bessel *B* map indicates regions of saturation, in our shortest exposures. (A color version of this figure is available in the online journal.)

than average fractional polarization, leading to intrinsically higher polarimetric SNR. However, it is possible that our spatial resolution of 5.″76 "averages out" these features, which may only exist on small scales. In any case, it appears that our measurements are sampling the "thermal noise of the corona" (Inhester 2015), with no evidence of any other structure.

5. Conclusions

Observations obtained with the RIT Polarization Imaging Camera of the 2017 total Solar eclipse represent some of the best measurements of this sort to date. Polarization sensors appear well suited to these observing campaigns, which often involve travel to remote sites and a high degree of automation. The snapshot capability, especially, has proven its utility during this campaign, due to the presence of low, thin, fast moving clouds above Madras, Oregon.

Nevertheless, some challenges remain to be solved. Our measurements cannot easily be used to calculate the polarized brightness, *pB*, in absolute radiometric units ($\mathrm{W\,m^{-2}\,s^{-1}\,nm^{-1}}$), because we cannot easily determine the atmospheric transmission, at the time of totality. Going forward, it may be useful to observe a star of known brightness, in the vicinity of the Sun, to calibrate the transmission of the atmosphere. Similarly, contemporaneous measurements over a larger field of view may be useful to better measure the sky foreground near the corona.

The authors acknowledge the support and funding provided by Moxtek, Inc. In particular, we thank Ray West and Roger Ketcheson. We thank Dr. Peter Zimmer for providing access to the observing site in Madras, Oregon and Dr. Billy Vazquez for supplying the telescope mount used for this work. Lastly, we thank the referee for a thoughtful and helpful review of this manuscript.

Appendix
Demonstration of Instrumental Performance With Lunar Polarimetry

In preparation for the eclipse observations, we performed several days of Lunar polarimetry, to evaluate the performance of our polarimeter and estimate the proper exposure times. As part of this effort, we observed the Moon near full and half illumination, in the Bessel *B*, *V*, and *R* color filters. Our estimation of the DOLP and AOLP for the moon near half phase is shown in Figure 16. In these maps, pixels with polarimetric signal-to-noise <1 have been suppressed. Nevertheless, a strong halo of scattered light can be seen around the Lunar limb. The polarization of this light is mostly preserved, especially the AOLP. Furthermore, the measurements are consistent between the different color channels, in particular the AOLP, which does not change by more than $\sim 1^\circ$.

To estimate the sensitivity of our polarization camera for weak polarization features, we observed the Moon near full illumination, with a scattering angle $\alpha \sim$ few $^\circ$. The resulting maps of DOLP and AOLP are shown in Figure 17.

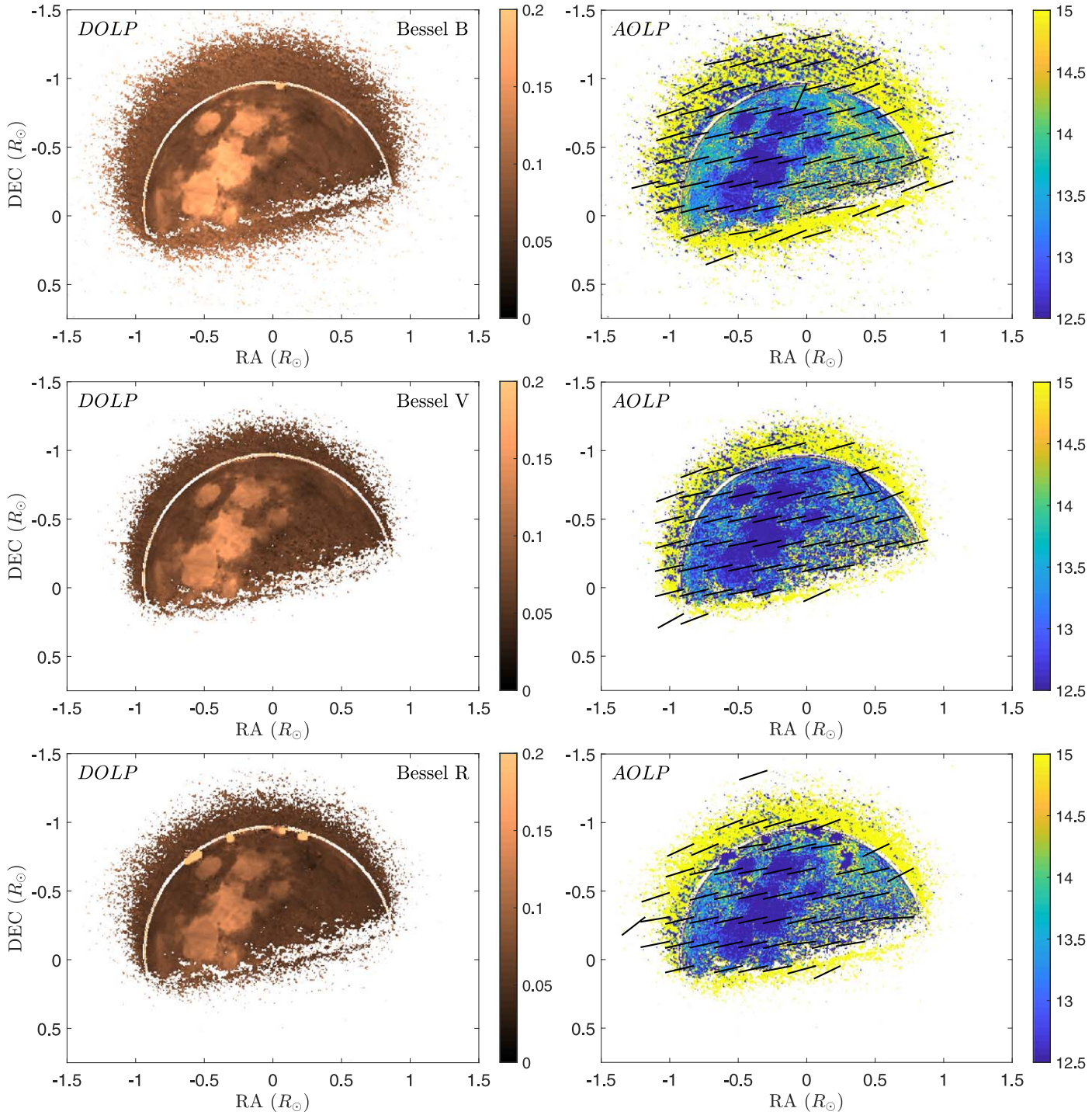

Figure 16. Linear polarimetry of the Moon in the *B*, *V*, and *R* filters. At ∼half phase, the scattering angle, α, is near 90° and the polarization peaks at ∼20% in the marae regions. Though the degree of linear polarization depends on wavelength, the angle of linear polarization is consistent to within ∼1°. Here the angle of linear polarization is given in the instrumental reference frame.
(A color version of this figure is available in the online journal.)

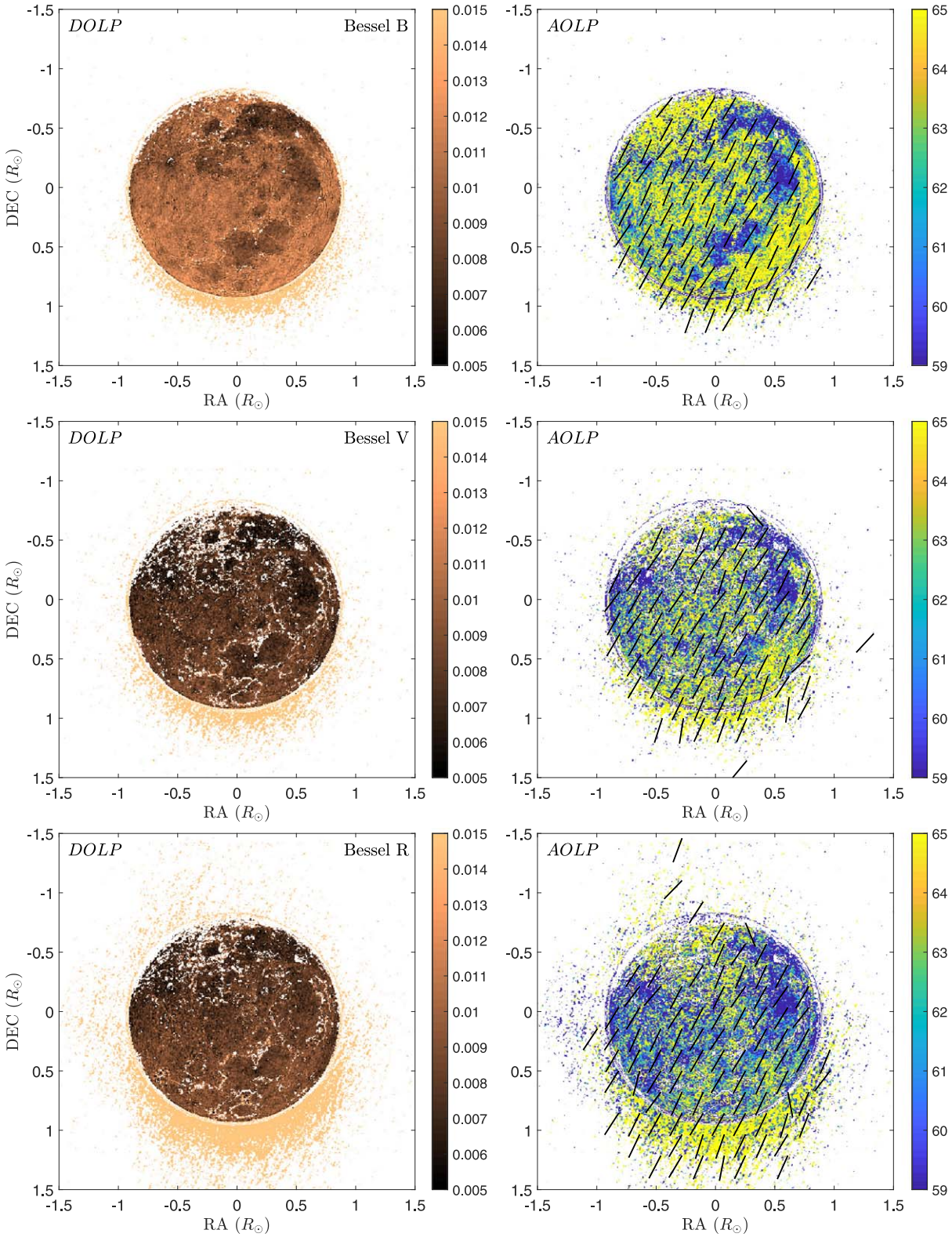

Figure 17. Linear polarimetry of the Moon in the *B*, *V*, and *R* filters. At ∼full phase, the scattering angle, α, is near 0° and the polarization peaks at ∼1.5% in the highland regions, in contrast to the measurements made at half phase.
(A color version of this figure is available in the online journal.)

ORCID iDs

Dmitry Vorobiev https://orcid.org/0000-0002-1498-5811

References

Arago, F. 1856, Popular Astronomy, Vol. 3 (Paris: GIDE and J. BAUDRY)
Bajorski, P. 2011, Statistical Models (New York: Wiley), 85
Brock, N., Kimbrough, B. T., & Millerd, J. E. 2011, Proc. SPIE, 8160, 81600W
Brueckner, G. E., Howard, R. A., Koomen, M. J., et al. 1995, SoPh, 162, 357
Dandekar, B. S., & Turtle, J. P. 1971, ApOpt, 10, 1220
Eshelman, L. M. 2018, PhD dissertation, Montana State Univ.
Eshelman, L. M., Tauc, M. J., Hashimoto, T., et al. 2018, Proc. SPIE, 10655, 106550L
Inhester, B. 2015, arXiv:1512.00651
Kim, I. S., Nasonova, L. P., Lisin, D. V., Popov, V. V., & Krusanova, N. L. 2017, JGRA, 122, 77
Koutchmy, S., Molodenskii, M. M., Nikol'Skii, G. M., & Filippov, B. P. 1993, ARep, 37, 286
Koutchmy, S., & Schatten, K. H. 1971, SoPh, 17, 117
Minnaert, M. 1930, ZA, 1, 209
Molodensky, M. M. 1973, SoPh, 28, 465
Nordin, G. P., Meier, J. T., Deguzman, P. C., & Jones, M. W. 1999, JOSAA, 16, 1168
Pomozi, I., Gál, J., Horváth, G., & Wehner, R. 2001, RSEnv, 76, 181
Qu, Z. Q., Deng, L. H., Dun, G. T., et al. 2013, ApJ, 774, 71
Quémerais, E., & Lamy, P. 2002, A&A, 393, 295
Shaw, J. A., Eshelman, L. M., Tauc, M. J., & Shaw, G. E. 2019, Proc. SPIE, 11132, 111320C
Skomorovsky, V. I., Trifonov, V. D., Mashnich, G. P., et al. 2012, SoPh, 277, 267
Snik, F., Craven-Jones, J., Escuti, M., et al. 2014, Proc. SPIE, 9099, 90990B
Tyo, J. S., Goldstein, D. L., Chenault, D. B., & Shaw, J. A. 2006, ApOpt, 45, 5453
van de Hulst, H. C. 1950, BAN, 11, 135
Vorobiev, D. V., Ninkov, Z., & Brock, N. 2018, PASP, 130, 064501